



HAL
open science

1310 nm hybrid InP/InGaAsP on silicon distributed feedback laser with high side-mode suppression ratio

Hélène Duprez, Antoine Descos, Thomas Ferrotti, Corrado Sciancalepore, C. Jany, K. Hassan, Christian Seassal, S. Menezo, B. Ben Bakir

► **To cite this version:**

Hélène Duprez, Antoine Descos, Thomas Ferrotti, Corrado Sciancalepore, C. Jany, et al.. 1310 nm hybrid InP/InGaAsP on silicon distributed feedback laser with high side-mode suppression ratio. *Optics Express*, 2015, 23 (7), pp.8489-8497. 10.1364/OE.23.008489 . hal-01489445

HAL Id: hal-01489445

<https://hal.science/hal-01489445>

Submitted on 19 Apr 2019

HAL is a multi-disciplinary open access archive for the deposit and dissemination of scientific research documents, whether they are published or not. The documents may come from teaching and research institutions in France or abroad, or from public or private research centers.

L'archive ouverte pluridisciplinaire **HAL**, est destinée au dépôt et à la diffusion de documents scientifiques de niveau recherche, publiés ou non, émanant des établissements d'enseignement et de recherche français ou étrangers, des laboratoires publics ou privés.

Copyright

1310 nm hybrid InP/InGaAsP on silicon distributed feedback laser with high side-mode suppression ratio

Helene Duprez,¹ Antoine Descos,¹ Thomas Ferrotti,^{1,2} Corrado Sciancalepore,¹ Christophe Jany,¹ Karim Hassan,¹ Christian Seassal,³ Sylvie Menezo,¹ and Badhise Ben Bakir^{1,*}

¹Univ. Grenoble Alpes, CEA, LETI, MINATEC campus, CEA-Grenoble, F38054 Grenoble, France

²ST Microelectronics, 850 rue Jean Monnet, 38920 Crolles, France

³Université de Lyon, Institut des Nanotechnologies de Lyon-INL, UMR CNRS 5270, CNRS, Ecole Centrale de Lyon, Ecully F-69134, France

*badhise.ben-bakir@cea.fr

Abstract: We report on the design, fabrication and performance of a hetero-integrated III-V on silicon distributed feedback lasers (DFB) at 1310 nm based on direct bonding and adiabatic coupling. The continuous wave (CW) regime is achieved up to 55 °C as well as mode-hop-free operation with side-mode suppression ratio (SMSR) above 55 dB. At room temperature, the current threshold is 36 mA and the maximum coupled power in the silicon waveguide is 22 mW.

©2015 Optical Society of America

OCIS codes: (250.5300) Photonic integrated circuits; (140.5960) Semiconductor lasers.

References and links

1. M. Asghari and A. V. Krishnamoorthy, "Silicon photonics - Energy efficient communication," *Nat. Photonics* **5**(5), 268–270 (2011).
2. A. V. Krishnamoorthy, R. Ho, X. Zheng, H. Schwetman, J. Lexau, P. Koka, G. Li, I. Shubin, and J. E. Cunningham, "Computer systems based on silicon photonics interconnects," *Proc. IEEE* **97**(7), 1337–1361 (2009).
3. H. Rong, R. Jones, A. Liu, O. Cohen, D. Hak, A. Fang, and M. Paniccia, "A continuous-wave Raman silicon laser," *Nature* **433**(7027), 725–728 (2005).
4. R. E. Camacho-Aguilera, Y. Cai, N. Patel, J. T. Bessette, M. Romagnoli, L. C. Kimerling, and J. Michel, "An electrically pumped germanium laser," *Opt. Express* **20**(10), 11316–11320 (2012).
5. S. Stanković, R. Jones, M. N. Sysak, J. M. Heck, G. Roelkens, and D. V. Thourhout, "Hybrid III-V/Si Distributed-Feedback Laser Based on Adhesive Bonding," *IEEE Photon. Technol. Lett.* **24**(23), 2155–2158 (2012).
6. A. W. Fang, E. Lively, Y.-H. Kuo, D. Liang, and J. E. Bowers, "A distributed feedback silicon evanescent laser," *Opt. Express* **16**(7), 4413–4419 (2008).
7. M. N. Sysak, H. Park, A. W. Fang, J. E. Bowers, R. Jones, O. Cohen, O. Raday, and M. J. Paniccia, "Experimental and theoretical thermal analysis of a Hybrid Silicon Evanescent Laser," *Opt. Express* **15**(23), 15041–15046 (2007).
8. B. Ben Bakir, A. Descos, N. Olivier, D. Bordel, P. Grosse, E. Augendre, L. Fulbert, and J. M. Fedeli, "Electrically driven hybrid Si/III-V Fabry-Pérot lasers based on adiabatic mode transformers," *Opt. Express* **19**(11), 10317–10325 (2011).
9. B. Ben Bakir, C. Sciancalepore, A. Descos, H. Duprez, D. Bordel, L. Sanchez, C. Jany, K. Hassan, P. Brianceau, V. Carron, and S. Menezo, "Heterogeneously integrated III-V on Silicon Lasers," in *ECS*, **64**, 211–223 (2014).
10. M. S. Dahlem, C. W. Holzwarth, A. Khilo, F. X. Kärtner, H. I. Smith, and E. P. Ippen, "Reconfigurable multi-channel second-order silicon microring-resonator filterbanks for on-chip WDM systems," *Opt. Express* **19**(1), 306–316 (2011).
11. B. Ben Bakir, A. V. de Gyves, R. Orobtcouk, P. Lyan, C. Porzier, A. Roman, and J.-M. Fedeli, "Low-loss (< 1 dB) and polarization-insensitive edge fiber couplers fabricated on 200-mm silicon-on-insulator wafers," *IEEE Technology Lett.* **22**(11), 739–741 (2010).
12. M. Antelius, K. B. Gylfason, and H. Sohlström, "An apodized SOI waveguide-to-fiber surface grating coupler for single lithography silicon photonics," *Opt. Express* **19**(4), 3592–3598 (2011).
13. L. Liao, D. Samara-Rubio, M. Morse, A. Liu, D. Hodge, D. Rubin, U. Keil, and T. Franck, "High speed silicon Mach-Zehnder modulator," *Opt. Express* **13**(8), 3129–3135 (2005).
14. J. Van Campenhout, M. Pantouvaki, P. Verheyen, S. Selvaraja, G. Lepage, H. Yu, W. Lee, J. Wouters, D. Goossens, M. Moelants, W. Bogaerts, and P. Absil, "Low-voltage, low-loss, multi-Gb/s silicon micro-ring modulator based on a MOS capacitor," in *Optical Fiber Communication Conference*, OSA Technical Digest, paper OM2E.4.

15. L. Virost, P. Crozat, J.-M. Fédéli, J.-M. Hartmann, D. Marris-Morini, E. Cassan, F. Boeuf, and L. Vivien, "Germanium avalanche receiver for low power interconnects," *Nat Commun* **5**, 4957 (2014).
16. C. Sciancalepore, L. J. Richard, J.-A. Dallery, S. Pauliac, K. Hassan, J. Harduin, H. Duprez, U. Weidenmueller, D. F. G. Gallagher, S. Menezo, and B. Ben Bakir, "Low-crosstalk fabrication-insensitive echelle grating demultiplexers on silicon-on-insulator," *IEEE Photon. Technol. Lett.*, (published, in press), Dec. 04, 2014 (2014).
17. X. Sun, H.-C. Liu, and A. Yariv, "Adiabaticity criterion and the shortest adiabatic mode transformer in a coupled-waveguide system," *Opt. Lett.* **34**(3), 280–282 (2009).
18. L. A. Coldren, S. W. Corzine, and M. L. Masanovic, *Diode Lasers and Photonic Integrated Circuit* (Wiley, 2nd Edition, 2012), Chap. 3. (2009).
19. A. W. Fang, M. N. Sysak, B. R. Koch, R. Jones, E. Lively, Y. H. Kuo, D. Liang, O. Raday, and J. E. Bowers, "Single Wavelength Silicon Evanescent Lasers," *IEEE J. Quantum Electron.* **15**(3), 535–544 (2009).

1. Introduction

The need for high data transmission rates keeps increasing and this trend is unlikely to slow down in the foreseeable future. In this context, doubts are casted on the capability for current copper-based interconnects and electronics circuits to follow this tendency. Shrinking microelectronics nodes gets harder both because of the density limit and the heating managements within the circuits, which become increasingly expensive to cool. Power-efficient optical interconnects appear as a way to withstand the relentlessly growing bit stream.

The refractive index difference between silicon and its native oxide (SiO₂) is high enough to tightly confine an optical mode within silicon waveguide cores, consequently a great potential arises from this material for optical applications. Moreover, the interest for silicon photonics is growing [1,2], since it would leverage the know-how acquired within mature complementary metal oxide semiconductor (CMOS) technology in processing silicon. It appears as one of the most promising technology to functionally integrate photonic integrated circuits (PICs) with electronic driving devices on reduced footprints using 3D-CMOS processes.

Although silicon is a poor light emitter due to its indirect bandgap, making lasers out of silicon has been investigated during the last ten years showing promising results. The demonstration of a continuous wave silicon laser based on Raman scattering [3] incites to keep looking in this direction as well as the use of strained heavily doped Ge as a gain-enabler material [4]. However, both solutions need further development to be power-efficient.

One of the most mature wafer-level solutions to provide light to the PIC is to bond III-V-gain layers on silicon on insulator (SOI) wafers. The bonding can either be adhesive with polymers used as bonding layer [5], or direct using a thin silica layer to stick the III-V and the silicon wafers together via covalent SiO₂-SiO₂ low temperature bonding [6–9]. Light is thus generated and amplified in the III-V gain material and other optical functions, such as the laser feedback cavity, are implemented within the high-index-contrast SOI photonic circuitry. Such a design allows to easily integrate the hybrid optical source with other building blocks already demonstrated: optical resonators and filters [10], input/output (I/O) couplers [11,12], high-speed modulators [13,14], Si-Ge photodiodes [15], and wavelength (de)multiplexers [16].

One approach in III-V/Si laser architecture lies in designing the hybrid active region so that the optical mode stays mainly confined within the underlying silicon waveguide, interacting with the III-V quantum wells (QWs) only with its evanescent tail [5–7] which limits the modal gain. Though such a configuration is subject to less complexity regarding coupling, the amplification is restricted and the bonding layer thickness is critical. In our approach, we opted for a design that uses the III-V gain region as efficiently as possible by having the optical mode confined in the QWs [8, 9]. To allow for the mode to transit from the III-V to the silicon waveguide, adiabatic mode transformers were designed using the deterministic adiabaticity criterion demonstrated in [17].

We report herein hybrid III-V on silicon DFB lasers operating at 1310 nm based on direct bonding and adiabatic coupling between both materials. The article is organized as follows. Section 2 describes the laser architecture and the design of its different components with a numerical analysis for each of them, while the fabrication process is

outlined in section 3. The results, revealing the level of maturity of the heterogeneous III-V/Si DFB lasers in the O-Band, are given in section 4 focusing on the DFB laser static and thermal features.

2. Laser architecture and design

2.1 Overall structure

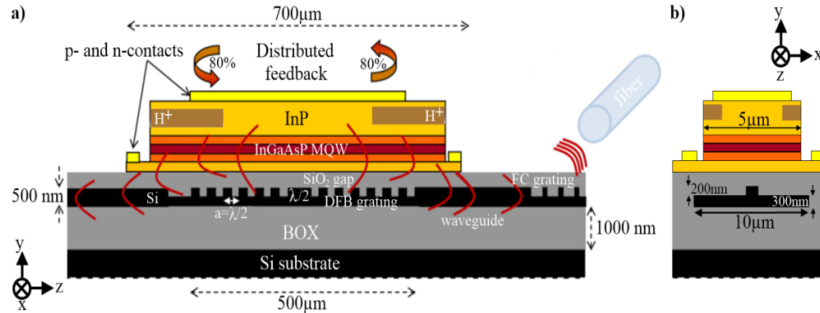


Fig. 1. Longitudinal (a) and transversal (b) schematics views of the laser. The III-V and the silicon waveguide are separated by a SiO₂ gap of 75 nm. The DFB grating is etched along the silicon waveguide underneath the III-V active layers. The active region consists in InGaAsP multiple QWs surrounded by *p*- and *n*-doped InP layers.

Schematic longitudinal and transversal cross-section views of the device are represented on Fig. 1. The III-V and the silicon waveguide are separated by a SiO₂ gap of 75 nm. The quarter-wave shifted (QWSh) DFB grating is etched along the 500-nm-thick silicon waveguide underneath the III-V active layers. The active region is 700-μm-long and consists of InGaAsP multiple QWs (MQWs) exhibiting maximum gain centered on 1310 nm, surrounded by *p*- and *n*-doped InP layers. The silicon rib is 200-nm-thick and needs to be narrow enough to confine the light mostly in the III-V QWs. The mode overlap with the MQWs and the barriers is calculated to be 0.35. In order to maximize the modal gain, carrier injection is concentrated in the center of the III-V active waveguide thanks to H⁺ “resistive” doping on the sides of the 5-μm-wide InP ridge. At both terminations of the grating, the silicon waveguide is widened adiabatically, enabling light to be coupled into the silicon with more than 90% efficiency, allowing as much optical power to be produced at both outputs of the laser. Those 100-μm-long mode transformers are a key point in the design of the device. Laser light emission is collected with a fiber positioned on the top of a waveguide-to-fiber surface grating coupler.

2.2 Adiabatic III-V to silicon transition

In order to obtain the optical mode coupling from the III-V to the silicon at the output of the gain region, an adiabatic taper is designed in the silicon waveguide as explained below [17]. Calculations of the effective indices are made with a two-dimensional (2D) finite elements method (FEM) solver, first for the isolated modes in the silicon waveguide and in the III-V, then for the modes of the coupled structure, referred to as supermodes. The normalized coupling constant (γ) is found as a function of the silicon waveguide width (W_{rib}):

$$\gamma(W_{\text{rib}}) = \frac{\delta(W_{\text{rib}})}{\kappa_{z_0}} \quad (1)$$

$$\delta = \frac{\beta_{\text{III-V}} - \beta_{\text{Si}}}{2} \quad (2)$$

$$\kappa_{z_0} = \frac{\beta_{\text{even}} - \beta_{\text{odd}}}{2} \quad (3)$$

where $\beta_{\text{III-V}}$, β_{Si} , β_{even} , β_{odd} , are the propagation constants defined as $\beta_i = 2\pi n_{\text{eff},i} / \lambda$ for the first mode in the III-V and in the silicon and for the two first supermodes (even and odd) in the coupled structure, respectively. z_0 corresponds to the position of the phase matching for the even supermode i.e. when the mode overlaps equally the silicon and the III-V regions of the coupled waveguide system. From Eq. (1-3), an interpolation leads to $W_{\text{rib}} = f(\gamma)$. The shape of the taper is then deduced from the adiabaticity criterion demonstrated in [17]:

$$\gamma(z) = \tan(\arcsin(u)) \quad (4)$$

$$u = 2\kappa_{z_0} \sqrt{\varepsilon(z-z_0)} \quad (5)$$

with ε the power penalty (i.e. the power radiated in the odd supermode) due to the transition. The lower ε is, the longer the transition needed to achieve such low power penalty.

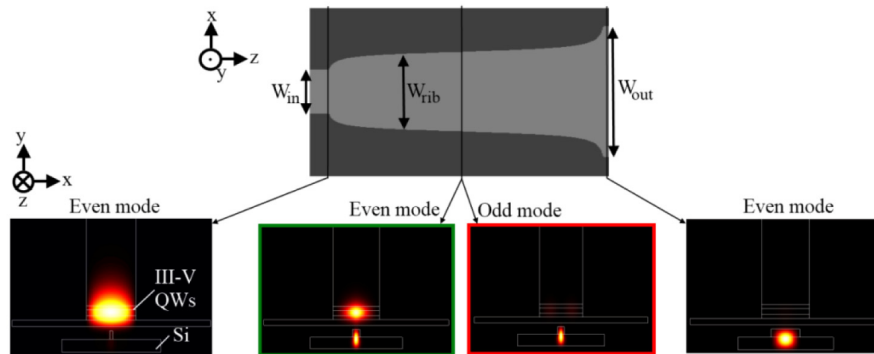


Fig. 2. Schematic top view of the adiabatic taper in the silicon rib and electric field distributions (E) at the input, output and middle of the taper for the even mode. The odd mode is represented at the middle: the taper is designed to get rid of this mode and have all the power in the even mode.

Once the shape is obtained, an optimization of the input and output width of the taper needs to be implemented. Figure 2 represents a schematic view of the taper with a picture of the calculated supermode at both ends: at the input it stays mainly confined within the III-V region showing a good overlap with the MQWs while at the output, the mode is very well confined in the silicon. Two insets are added in Fig. 2 displaying the field intensity of the even and odd supermodes at an intermediate width. The taper aims at transferring all the power in the even supermode and with only a few percent (ε) in the odd one. The taper coupling efficiency is calculated using a beam propagation method (BPM) solver leading to the coupling efficiency map shown in Fig. 3(a). It is important to have a robust design regarding parameters which depend strongly on fabrication processes. For this taper, the influence of the output width is very limited, while that of the input width is more important but remains within the process variations window. The adiabaticity of the taper is checked plotting the coupling efficiency as a function of the taper length as in Fig. 3(b). It shows that once the maximum coupling efficiency is reached, there is almost no back-coupling oscillation contrary to what is observed with directional couplers for instance. The remaining oscillations with amplitude ε are due to the coupling to the unwanted odd supermode.

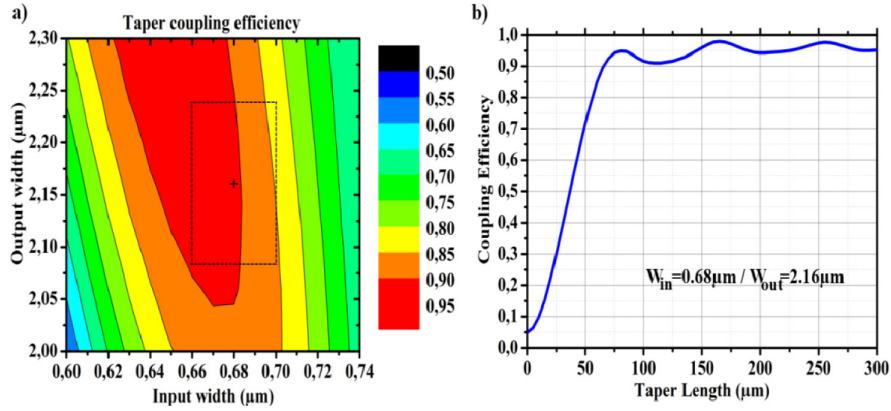


Fig. 3. (a) Taper coupling efficiency depending on the input and output width of the rib silicon waveguide. The cross represents the dimensions chosen and the dashed square stands for the process variation window. (b) Taper coupling efficiency as a function of the taper length with $W_{in} = 0.68\mu\text{m} / W_{out} = 2.16\mu\text{m}$.

2.3 Distributed-feedback cavity design

The cavity in the DFB is characterized by a grating underneath the active region where the top of the silicon waveguide is partially etched as represented on Fig. 4(a). Three parameters define the grating: the rib width, equal to the taper input width, the etching depth d and the period a . The optical mode being confined within the III-V along the cavity, the coupling strength between the grating and the mode needs to be determined to ensure a high enough cavity quality factor and achieve single-mode operation. This strength is described by the grating coupling constant (κ_r), calculated using the equation derived from [18]:

$$\kappa_r = \frac{2\Delta n_{\text{eff}}}{\lambda} \quad (6)$$

$$\Delta n_{\text{eff}} = n_{\text{eff}2} - n_{\text{eff}1} \quad (7)$$

where $n_{\text{eff}1}$ and $n_{\text{eff}2}$ are the effective indices of the coupled structure even mode when the silicon waveguide is or is not etched, as depicted in Fig. 4 (a).

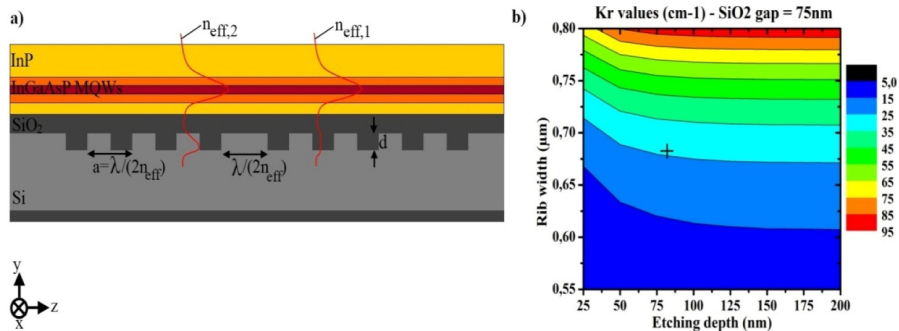


Fig. 4. (a) Schematic side view of the grating underneath the III-V active region with the $\lambda/(4n_{\text{eff}})$ defect in the middle of the grating. The modal repartition is represented when the Si waveguide is or is not etched. (b) Grating coupling constant (κ_r) calculated values. The cross represents the κ_r of our design (25.5 cm^{-1}).

Based on the calculated reflectivity for distributed Bragg reflector (DBR) lasers [18], the $\kappa_r L_g$ product is estimated to be within the 1-1.6 range for a DFB, L_g being the grating length. For a grating length of $500\mu\text{m}$, κ_r has then to fit between 20 cm^{-1} and 30 cm^{-1} . To determine such κ_r values, the even supermode refractive index of the coupled structure is

calculated using a FEM mode solver for different etching depths and silicon waveguide widths. The results are shown on Fig. 4(b). Above 70 nm of etching depth, the coupling strength evolution is insignificant. On the contrary, the silicon rib width has much more effect on κ_r . This trend was expected because the wider the silicon waveguide is, the stronger is the overlap for the mode with the DFB grating. For the laser described here, a width of 0.68 μm is selected which, for an 80 nm etching depth, leads to $\kappa_r = 25.5 \text{ cm}^{-1}$ and a $\kappa_r L_g$ value of 1.28, while the taper coupling efficiency stays between 90 and 100%. Using the same method, the grating coupling constant of the odd mode was calculated to be less than 0.2 cm^{-1} for these dimensions showing that the effect of the grating on this mode is much lower than on the even one.

A grating period of 202 nm was then calculated using the Bragg Law in order to operate at 1310 nm:

$$a = \frac{2\lambda}{n_{\text{eff}}} \quad (8)$$

with $\overline{n_{\text{eff}}}$ the average index in the coupled structure which include the grating. To avoid the mode degeneracy inherent to DFB gratings and achieving single-mode operation, a QWSh is designed in the middle of the grating represented by a $\lambda/(4n_{\text{eff}})$ defect as displayed on Fig. 4(a).

3. Laser fabrication

The laser front- to back-end processing can be summarized as follows. First, a 200-mm SOI wafer is processed with four successive 193-nm-deep UV (DUV) photolithography and reactive ion etching (RIE) steps. Figure 5 illustrates the first three steps. The 2nd and 3rd levels are defined using SiO_2 hard masks while photoresist is sufficient for the two other levels. First the DFB grating is etched, then the rib etching ensues. The third level corresponds to the definition of the fiber coupler grating. A last phase consists in separating all the lasers on the wafer, etching all the silicon left around the devices.

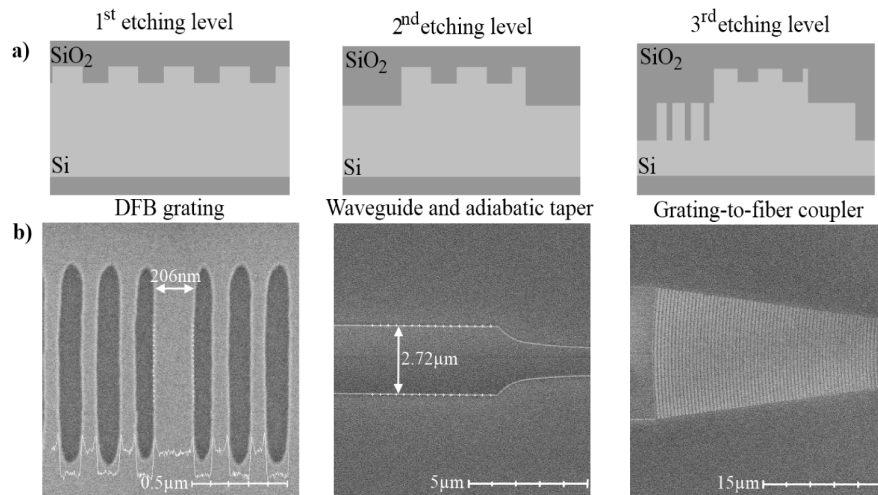


Fig. 5. (a) Schematic side views of the Si waveguide for the first three etching levels: the DFB grating, the rib waveguide with the adiabatic taper and the grating-to-fiber coupler (b) Corresponding top SEM view after each etching.

The patterned SOI wafer is encapsulated with 700 nm of SiO_2 afterward, followed by chemical-mechanical polishing (CMP) which allows planarisation of the wafer as well as aiming at the 75 nm SiO_2 gap. The III-V epitaxial structure to bond is depicted on Table 1 without the InP substrate. The MQWs are separated from the n - and p - layers by separated confinement layers (SCH) and superlattice layer are added within the n -contact

to prevent the defect propagation from the bonded interface to the QWs. Both the III-V and the SOI surfaces are activated through oxygen plasma and then put in contact at room temperature. Though room temperature bonding is sufficient to ensure bonding, a 180 minutes post-bonding annealing is performed at 200 °C to reinforce it. A picture of the bonded wafers is shown on Fig. 6(a). The subsequent steps comprise the InP substrate removal using HCl/H₂O wet etching, the H⁺ implantation and the wafer downsizing from 8 to 3 inches.

Table 1. III-V epitaxial growth layer structure

Layer	Material	Bandgap (eV)	Doping (cm ⁻³)	Thickness (nm)
p - contact layer	InGaAs	0.77	3x10 ¹⁹	200
Transition	InGaAsP	1.13	1x10 ¹⁹	50
p - cladding layer	InP	1.34	5x10 ¹⁸ →1x10 ¹⁹	1800
SCH	InGaAsP	1.13	undoped	100
MQW barriers (x7)	InGaAsP	1.13	undoped	10
MQWs (x8)	InGaAsP	0.95	undoped	8
SCH	InGaAsP	1.13	undoped	100
n - contact layer	InP	1.34	3x10 ¹⁸	110
Super-lattice (x2)	InGaAsP	1.13	3x10 ¹⁸	7.5
Super-lattice (x2)	InP	1.34	3x10 ¹⁸	7.5
Bonding interface	InP	1.34	undoped	10

The III-V waveguide is then defined with CH₄-H₂ dry etching followed by the *p*- and *n*-type contact deposition thanks to a lift-off method. Afterward, the 2-inches-wafer is covered by 3-μm-thick BCB polymers used as encapsulation layer which is open to reach the contacts and finally, TiPtAu metallic pad are deposited. An optical microscope picture displaying one of the devices at the end of the whole fabrication process is represented on Fig. 6(b).

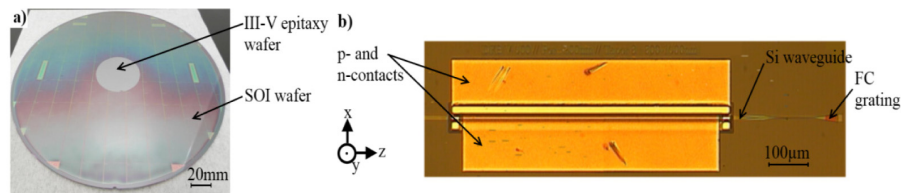


Fig. 6. (a) Picture of the III-V wafer bonded on the 200 mm SOI wafer (b) Optical microscope view of the laser.

4. Results

Laser operation with a classic DFB signature was demonstrated on the whole wafer, however a statistic study will be the object of future work and we chose here to focus on both static and thermal characteristics of one particular device. The chip was mounted on a Peltier module to set its temperature from 20°C up to 80°C. The output power was measured collecting the light from the surface grating coupler with a multimode fiber (MMF). Electrical pumping is ensured applying a positive bias on the *p*-contact of the laser. *L-I* curves in CW regimes for different temperatures are presented on Fig. 7, showing lasing effect up to 55 °C.

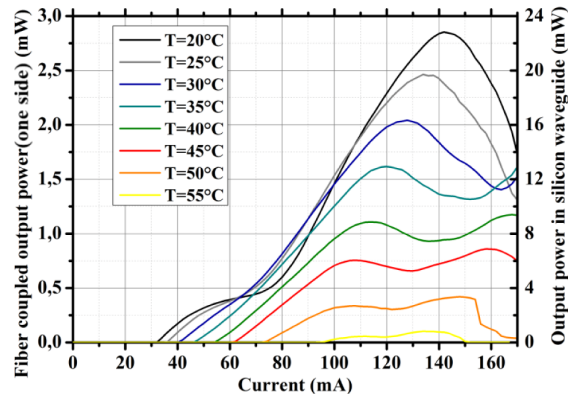


Fig. 7. L - I curves with increasing temperature. The left scale gives the output power in the fiber while the right scale gives the output power obtained in the waveguide.

As represented on Fig. 8(a), the room temperature (RT) threshold current is 36 mA which corresponds to a $1.03\text{kA}/\text{cm}^2$ current density for a $700\text{-}\mu\text{m}$ -long and $5\text{-}\mu\text{m}$ -wide active region. The maximum output power is then 2.8 mW in the waveguide. The fiber coupling losses were measured to be 6 dB. We can therefore conservatively assess an output power of 11 mW coupled into the silicon waveguide and 22 mW if we consider both outputs. The L - I slope being $0.24\text{W}/\text{A}$, the resulting differential quantum efficiency of the laser is 25%. Moreover, the laser diodes are characterized by a turn-on voltage of 1.23 V and a series resistance of $10.5\ \Omega$.

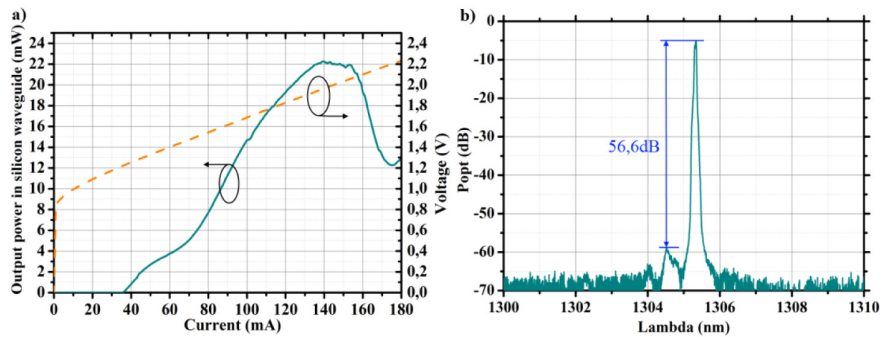


Fig. 8. Room-temperature LIV (a) and spectrum of the laser at $I = 107\text{mA}$ (b). The resolution of the optical spectrum analyser (OSA) was $0.02\ \text{nm}$.

Figure 8(b) displays the laser emission spectrum at 107 mA driving current at RT. Single-mode operation is reached with more than 56 dB of side mode suppression ratio (SMSR) which is the highest value for III-V/Si DFB lasers to the best of our knowledge. As shown in Fig. 9(a), the device operates single-mode over a current range of 170 mA until the very end of the roll-off region for different stage temperatures ($25\ ^\circ\text{C}$, $35\ ^\circ\text{C}$, $45\ ^\circ\text{C}$, $55\ ^\circ\text{C}$). Such a structure might allow competition between the even and odd mode and the fact that the spectrum is mode-hop-free proves that the taper is adiabatic and gets rid of the odd mode, as expected. Furthermore, such a spectral purity demonstrates the uniformity of the grating and the QWSh. Had there been other defects in addition to the QWSh in the grating, modal competition with other defect-modes may have been observed.

To complete the thermal analysis, measurements were implemented in pulsed regime (0.1% duty cycle and 1 ms pulse repetition) to limit heating from self-induced power dissipation in the laser. Measurements of the threshold for each temperature from $15\ ^\circ\text{C}$ to $75\ ^\circ\text{C}$ led to a characteristic temperature T_0 of $44\ ^\circ\text{C}$ which is coherent with the fact that the laser effect stops for temperatures higher than $60\ ^\circ\text{C}$. A linear fit of the peak wavelength shift versus stage temperature in pulsed regime gives $(\Delta\lambda/\Delta T)_{\text{DC}0.1\%,1\text{ms}} = 0.08$

nm/°C as shown in Fig. 9(b). Since the peak wavelength shift versus dissipated power in CW regime is $(\Delta\lambda/\Delta P)_{CW} = 3.72\text{nm/W}$ (Fig. 9(c)), the thermal impedance, defined as the ratio of both values, is $Z_T = 44.1^\circ\text{C/W}$.

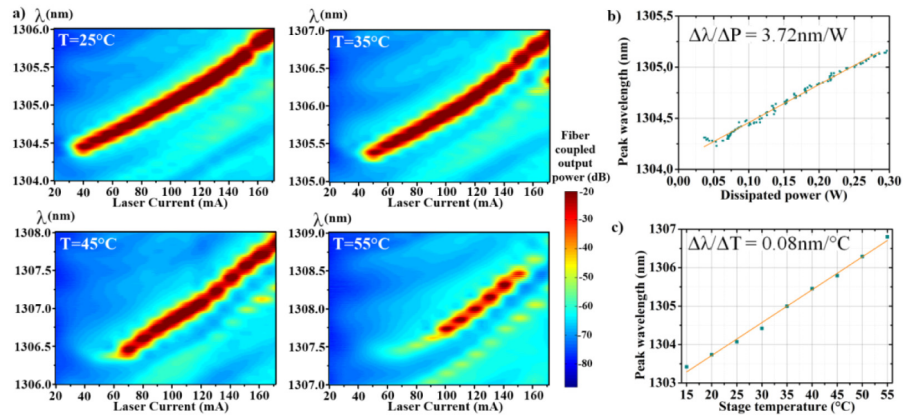


Fig. 9. (a) Laser spectra as a function of the pumping current for various stage temperatures: 25°C, 35°C, 45°C and 55°C Laser peak wavelength as a function of the dissipated power (CW) (b) as well as of the stage temperature in pulsed regime (c).

5. Conclusion

This work reports on the recent breakthroughs toward the maturity of III-V on Silicon lasers emitting in the O-band for datacom applications. A 700- μm -long QWSh distributed feedback laser was demonstrated operating in the continuous-wave regime up to 55°C, with a current threshold of 36 mA at 25°C and maximum output power of 22 mW available for the Si-PIC transmitter. The investigation is extended to a thermal analysis showing a laser characteristic temperature of 44°C and a laser thermal impedance of 44.1 °C/W.

Current and future works are mainly focused on the improvement of maximum operation temperature, refining the fabrication process, and the co-integration of the laser either with a III-V on silicon electro-absorption modulator or with a SOI Mach-Zender modulator. Development of the whole process on the 200-mm-platform as well as 3D wafer-level packaging are ongoing.

Acknowledgments

The authors would like to thanks K. Ribaud and P. Grosse for their help on device characterization. This work was supported by the French national program ‘programme d’Investissements d’Avenir’, IRT Nanoelec ANR-10-AIRT-05.